ADVANCED SCIENCE
Open Access
www.advancedscience.com

High Conversion Efficiency in Intrinsic High Power-Density Mg_2Sn-GeTe Thermoelectric Generator

*Xinzhi Wu, Longquan Wang, Airan Li, Gang Wu, Zhao Hu, Fei Frank Yun, and Takao Mori**

Thermoelectric generators (TEGs) offer a sustainable solution for thermal energy harvesting, where maximizing energy output necessitates achieving both high power density and high conversion efficiency. However, TEGs with intrinsically high power density by employing high power factor materials often face efficiency limitations due to their usually high thermal conductivity. Here, intrinsically high power density TEGs based on Mg_2Sn-GeTe for the first time is presented, simultaneously delivering a remarkable conversion efficiency of 9% under a temperature gradient of 418 K, thereby setting a new benchmark in the field. This exceptional performance is attributed to the significant balance between the moderating carrier and phonon transport in Mg_2Sn, enabled by a stepwise aliovalent Sb and Bi solid solution, without over-compromising its outstanding power factor. Consequently, a high thermoelectric figure of merit of 1.4 is achieved in $Mg_2Sn_{0.8}(Sb_{0.5}Bi_{0.5})_{0.2}$. The high-performance Mg_2Sn–GeTe TEGs introduced here represent a significant advancement in thermoelectric technology, offering an innovative and efficient solution for off-grid energy supply in waste-heat-rich environments.

1. Introduction

Industrial processes are a major source of waste heat, with up to 60% of energy often lost as residual heat, exacerbating environmental concerns.[1] Coupled with the ongoing global energy crisis, the increasing environmental challenges, and the urgent push toward carbon neutrality and peak emissions targets, there is an escalating demand for sustainable energy conversion technologies.[2,3] Thermoelectric generators (TEGs) present a promising solution, as they directly convert heat into electricity without producing emissions or noise, offering a clean and efficient method for energy recovery.[4,5] This is especially relevant in scenarios with abundant heat sources, where TEGs can promisingly address energy and environmental challenges.[4]

To expand their applicability across diverse heat-rich environments, enhancing the energy output of TEGs is crucial, as it directly determines their capability to meet varied power demands.[6] Maximizing the energy output of TEGs requires both high power density and high conversion efficiency. Power density ensures the amount of energy generated per unit area, while conversion efficiency dictates how effectively heat is converted into electrical energy and minimizes energy losses. Power density is primarily influenced by the power factor of thermoelectric (TE) materials, while conversion efficiency is determined by the thermoelectric figure of merit (ZT) without considering device size and interfaces.[7] Interfacial resistance has long posed a bottleneck for device advancement,[8] and encouragingly, recent advances have significantly mitigated this issue, reducing interfacial resistivity to as low as 10 $\mu\Omega\cdot cm^2$,[9–12] which limits ZT losses below 5%.[13] TEGs with high power density hold unique advantages in practical application for waste heat recovery, such as in industrial environments or automotive exhaust heat recovery.[14] Choosing TE materials with a high power factor can facilitate the development of high-power-density TEGs. However, the usually high thermal conductivity of such TE materials often leads to a reduced ZT, ultimately lowering the conversion efficiency of these TEGs. For instance, some typical materials NiAu, Fe_2VAl, NbFeSb, Mg_2Sn, etc.[15–17] Therefore, balancing the trade-off between the electrical power factor and thermal conductivity via moderating carrier and phono transport remains a significant challenge in developing TEGs with high power density and conversion efficiency.

The n-type Mg_2Sn-based[18–27] and p-type GeTe-based[28–31] compounds stand out as promising candidates for power-oriented TEGs due to their high power factor, which grants them intrinsic advantages in achieving high power density in mid-temperature applications. Additionally, their environmentally friendly composition makes them sustainable options. The p-type GeTe has garnered significant attention for its high power

---

X. Wu, L. Wang, A. Li, G. Wu, Z. Hu, F. F. Yun, T. Mori
Research Center for Materials Nanoarchitectonics (MANA)
National Institute for Materials Science (NIMS)
Tsukuba 305–0044, Japan
E-mail: mori.takao@nims.go.jp
Z. Hu, T. Mori
Graduate School of Pure and Applied Science
University of Tsukuba
1-1-1 Tennodai, Tsukuba, Ibaraki 305–8671, Japan

The ORCID identification number(s) for the author(s) of this article can be found under https://doi.org/10.1002/advs.202506997

DOI: 10.1002/advs.202506997

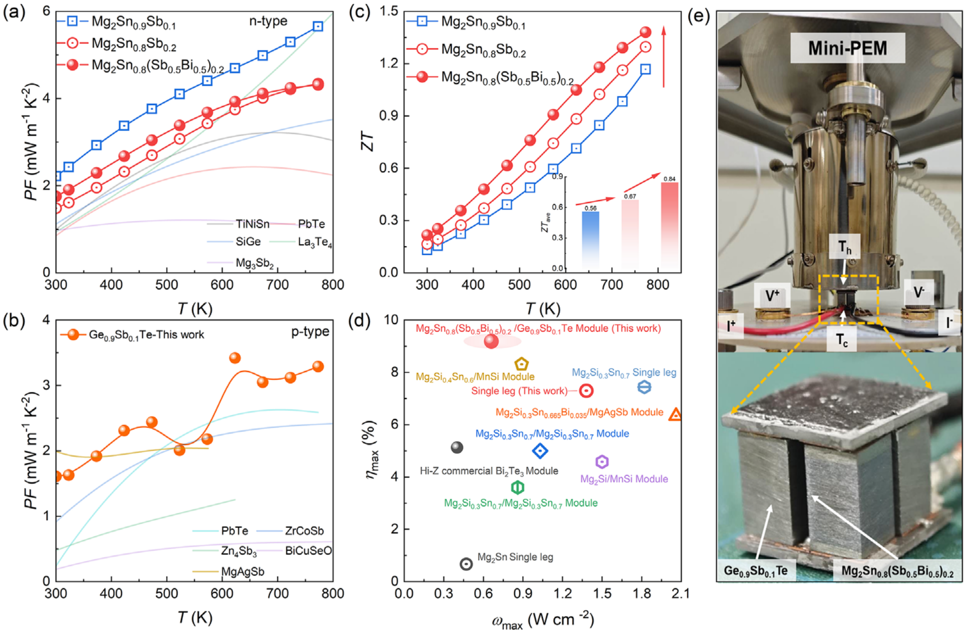

Figure 1. Stepwise Optimized performance of TE materials and device via aliovalent solid solution Strategy. The temperature-dependent power factor variations for n-type Mg_2Sn a) and p-type GeTe b), compared to several benchmark TE materials.[41] c) ZT values as a function of temperature, and the inset shows the ZT_{ave} values over the temperature range from room temperature to 773 K. d) A 2D map correlating the maximum power density (ω_{max}) with the maximum conversion efficiency (η_{max}) for Mg_2Sn-based TE devices, along with comparative data from the literature.[42–47] e) Photograph of the device setup in the commercial instrument Mini-PEM, with a close-up view of the device configuration.

factor and further reduced low thermal conductivity by entropy, defect or charge transfer engineering, with numerous reports demonstrating a ZT value exceeding 2.[32–36] However, the progress in enhancing the ZT of Mg_2Sn has lagged behind that of GeTe. Zaitsev et al.[18] first reported a ZT of 1.1 at 723 K in 2006, with subsequent enhancements to ZT 1.4 and a power factor of 5 W m^{-1} K^{-2}.[20,37] Since then, interest in Mg_2Sn has surged, culminating in recent breakthroughs,[19,20,24,38,39] achieving ZT 1.6 for $Mg_2(Si_{0.4}Sn_{0.6})_{0.985}Sb_{0.015}$ at 823 K.[40] However, experimental validation of these high-ZT materials at the device level remains unreported. Despite its inherently high power factor, the Mg_2Sn exhibits a thermal conductivity of over 5 W m^{-1} K^{-1} ≈300 K, which imposes a fundamental constraint on the conversion efficiency of fabricated TEGs. Nevertheless, addressing the intrinsic high thermal conductivity of n-type Mg_2Sn while maintaining high power density remains an overlooked challenge at the device level. To date, no practical implementation of p-n TEGs integrating these two high-power-factor TE materials has been reported.

In this study, we present a novel Mg_2Sn—GeTe TEGs with the intrinsic high-power-density, achieving an impressive conversion efficiency of 9% under a temperature gradient of 418 K. This performance is realized through a stepwise aliovalent Sb and Bi solid solution strategy on Mg_2Sn, which effectively balances the power factor and thermal conductivity via moderating carrier and phono transport, achieving a low lattice thermal conductivity of 1.8 W·m^{-1}·K^{-1} and a peak ZT of 1.4. Notably, this optimization entails only a ≈20% reduction in power factor, yet yields a ~47% decrease in lattice thermal conductivity—an outcome that substantially improves ZT and offers a promising route toward an intrinsic high-power-density system. These advancements address the inherent trade-off between electrical properties and thermal conductivity, culminating in a high-performance $Mg_2Sn_{0.8}(Sb_{0.5}Bi_{0.5})_{0.2}$–$Ge_{0.9}Sb_{0.1}Te$ TEG. Our optimized TEGs provide a sustainable and efficient solution for energy harvesting in waste-heat-rich, mid-temperature environments, offering a practical reference for other intrinsic high-power density TE devices.

2. Main Text

2.1. Stepwise Optimized Materials and Device Performance

Drawing inspiration from the intrinsic advantages of high power, we demonstrate a strategy that effectively balances the power factor and thermal conductivity through aliovalent solid solutions Sb and Bi in Mg_2Sn-based TE materials, leading to significantly improved ZT. As shown in **Figure** 1a, the power factor of $Mg_2Sn_{0.9}Sb_{0.1}$ reaches ≈7 mW m^{-1} K^{-2} at 773 K. Under similar Sb doping concentration, the power factor of $Ge_{0.9}Sb_{0.1}Te$ with high ZT exceeds ≈3 mW m^{-1} K^{-2} at 773 K, also surpassing most conventional p-type TE materials[41] such as PbTe, ZrCoSb, Zn_4Sb_3, BiCuSeO, and MgAgSb[48] (Figure 1b), thereby providing a fundamental requirement for high-power-density devices. However, the ZT of Mg_2Sn-based TE materials with an average ZT_{ave} of 0.56 for $Mg_2Sn_{0.9}Sb_{0.1}$ remains lower than that of GeTe (Figure S1, Supporting Information), As shown in Figure 1c, increasing the Sb doping concentration raises the ZT_{ave} from 0.56 for $Mg_2Sn_{0.9}Sb_{0.1}$ to 0.67 for $Mg_2Sn_{0.8}Sb_{0.2}$. Similarly, the peak power factor decreases from over 7 mW m^{-1} K^{-2} to ≈5 mW m^{-1} K^{-2} as Sb doping concentration increases from 0.1 to 0.2. Nevertheless, at Sb = 0.2, the peak power factor remains higher than that of other n-type TE materials[41] such as TiNiSn, SiGe, PbTe,

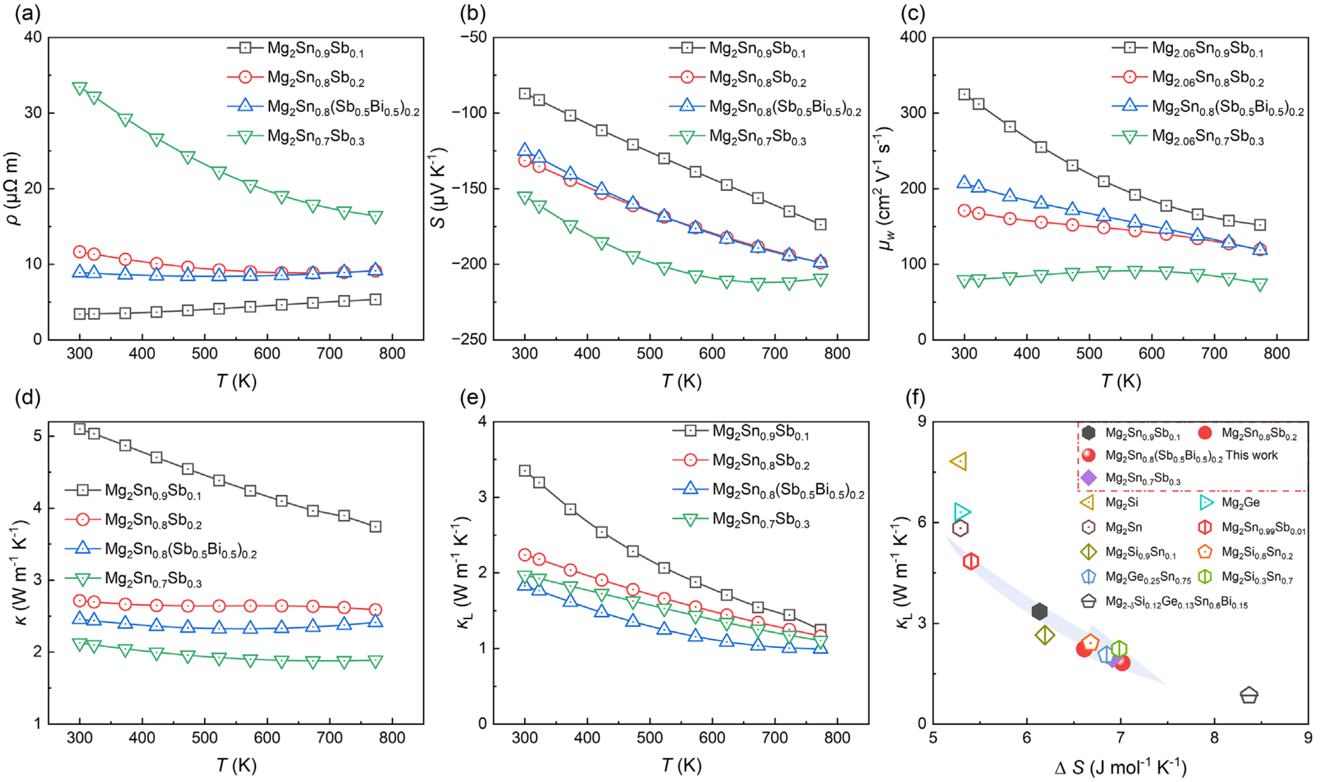

Figure 2. TE properties of Mg_2Sn-based materials. a–c) Temperature dependence of electrical resistivity (ρ), Seebeck coefficient (S), and weighted mobility (μ_w) for various compositions. (e) The temperature-dependent thermal conductivity κ, and lattice κ_L. f) The relationship between κ_L and configuration entropy (ΔS), along with comparative data from the literature.[23]

La_3Te_4, and Mg_3Sb_2, making it an ideal baseline for further optimizing its thermal conductivity (Figure 1a).

The addition of Bi raises the average ZT_{ave} to 0.84 in $Mg_2Sn_{0.8}(Sb_{0.5}Bi_{0.5})_{0.2}$ (Figure 1c), even with a slight improvement in the power factor compared with the $Mg_2Sn_{0.8}Sb_{0.2}$ (Figure 1a), particularly between room temperature to 773 K temperature range. The ZT of the repeated batches exhibits fluctuations within 5%, confirming the reliability of our findings (Figure S2, Supporting Information). The assembled 2 pair $Mg_2Sn_{0.8}(Sb_{0.5}Bi_{0.5})_{0.2}$-$Ge_{0.9}Sb_{0.1}Te$ device and the testing setup are shown in Figure 1d,e, demonstrating a power density of 0.7 W cm^{-2} and conversion efficiency of 9%. It is worth noting that the power density is also affected by the device's physical dimensions, suggesting that further improvements could be achieved through structural optimization of the TE device. In addition, the integration with p-type $Ge_{0.9}Sb_{0.1}Te$ results in significantly enhanced conversion efficiency, which is higher than that of other Mg_2Sn-based TEGs such as $Mg_2Si_{0.3}Sn_{0.7}$-$Mg_2Si_{0.3}Sn_{0.7}$,[43,46] Mg_2Si-MnSi,[42] and $Mg_2Si_{0.3}Sn_{0.7}$-MgAgSb TEGs.[47]

2.2. TE Performance

Sb and Bi play a pivotal role in optimizing the ZT of Mg_2Sn, necessitating a detailed investigation of their individual effects. In this section, we elucidate the underlying mechanisms of Sb and Bi aliovalent solid solution, specifically the Bi-induced retention of power factor and the Sb/Bi-driven reduction in thermal conductivity. This analysis highlights the delicate balance between moderating carrier transport to mitigate power factor degradation and enhancing phonon scattering to suppress thermal conductivity.

XRD and SEM analyses confirm the phase purity and compositional uniformity of the Sb- and Bi-doped samples (Figures S3–S6, Supporting Information), consistent with the high solubility of these elements in the Mg_2Sn matrix.[23,49,50] **Figure 2a–d** illustrates the electrical transport properties of the Mg_2Sn aliovalent element solid solution system. As shown in Figure 2a, the temperature-dependent electrical resistivity (ρ) curves reveal a distinct transition in conduction behavior. At Sn = 0.9, the system exhibits degenerate semiconductor behavior, characterized by a decreasing ρ with increasing temperature, indicative of metallic conduction. In contrast, as the Sn content decreases to 0.7, the material transitions to non-degenerate semiconductor behavior, with ρ showing a stronger temperature dependence, characteristic of thermally activated transport. Figure 2b presents the Seebeck coefficient (S), which increases monotonically with temperature for all compositions. Notably, the S also shows a general increase with higher Sb content. However, the power factor decreases systematically with decreasing Sn content, indicating that lower Sn concentrations adversely affect the overall electrical performance (Figure 1a). This trend suggests that electrical properties are strongly influenced by the Sn and Sb/Bi content.

Sb doping induces a non-monotonic evolution in carrier effective mass, extracted from Pisarenko analysis: effective mass increases from ≈2.9 m_e to ≈3.4 m_e at Sb = 0.2, then slightly decreases to ≈3.1 m_e at Sb = 0.3 (Figures S7, Supporting Information). This mirrors trends in Bi-doped Mg$_2$Sn, likely attributed to band structure changes driven by heavy and light band convergence.[49] To elucidate the mechanisms underlying these observations, the weighted mobility (μ_w) was analyzed using Snyder's modified model:[51]

$$\mu_w = \frac{3h^3\sigma}{8\pi e\left(2m_e k_B T\right)^{3/2}}\left[\frac{\exp\left[\frac{|S|}{k_B/e}-2\right]}{1+\exp\left[-5\left(\frac{|S|}{k_B/e}-1\right)\right]} + \frac{\frac{3}{\pi^2}\frac{|S|}{k_B/e}}{1+\exp\left[5\left(\frac{|S|}{k_B/e}-1\right)\right]}\right] \tag{1}$$

Where σ is experimental measurements of electrical conductivity, k_B is the Boltzmann constant, h is the Planck constant, e is the electron charge, and m_e is the free electron mass. The μ_w exhibits significant variations, particularly around room temperature, where it decreases as the Sn content decreases (Figure 2c). This trend suggests that μ_w could be a key factor influencing ρ, aligning with grain boundary scattering mechanisms commonly observed in Mg$_2$Si, Mg$_3$Sb$_2$, and half-Heusler TE materials.[52,53] The μ_w is related to the μ_H and the m^* by the relation $\mu_w \propto \mu_H/(m^*/m_e)^{3/2}$.[51] Across the Mg$_2Sn_{1-x}Sb_x$ series, the m^* exhibits a slight variation (2.9-3.4 m_e), whereas μ_H decreases sharply from 43.7 to 11.1 4 cm^2 V^{-1} s^{-1} as Sb content increases from $x = 0.1$ to 0.3, consistent with the corresponding drop in μ_w from 324.7 to 79.4 4 cm^2 V^{-1} s^{-1} (FiguresS 8). It should be noted that μ_H is also influenced by the band structure of the material. According to the relationship $\mu_H \propto \tau/m^*$, the reduction in μ_H arises from the combined effects of changed effective mass and carrier scattering. In other words, the varied band structure with increasing Sb content affects the μ_H. In addition, enhanced carrier scattering at higher Sb concentrations also contributes to decreased carrier mobility in Mg$_2$Sn as the Sb content increases.

Figure 2d-f presents the systematic variations in thermal properties. The thermal conductivity (κ) exhibits a decreasing trend with Sb increases (Figure 2d). A monotonic reduction in κ is observed with decreasing Sn content from Mg$_2$Sn$_{0.9}$Sb$_{0.1}$ to Mg$_2$Sn$_{0.8}$Sb$_{0.7}$. For example, the κ decreases from 5.1 W m^{-1} K^{-1} for Mg$_2$Sn$_{0.9}$Sb$_{0.1}$ to 2.1 W m^{-1} K^{-1} for Mg$_2$Sn$_{0.7}$Sb$_{0.3}$ at room temperature. In the Mg$_2$Sn$_{0.8}$(Sb$_{0.5}$Bi$_{0.5}$)$_{0.2}$, room-temperature κ is ≈2.4 W m^{-1} K^{-1}, which is slight lower than the value of Mg$_2$Sn$_{0.8}$Bi$_{0.2}$ (2.7 W·m^{-1} K^{-1}). The lattice conductivity (κ_L) is plotted after subtracting the electronic contribution. With increasing Sb content, κ_L deviates from the T^{-1} temperature dependence typical of phonon-phonon scattering, indicating the dominance of strong phonon scattering from point defects and grain boundaries introduced by Sb/Bi solid solution (Figure 2e). Sound velocity measurements support these observations, showing a clear reduction with increasing Sb/Bi content. The sound velocity decreases from 3005 m s^{-1} for Mg$_2$Sn$_{0.9}$Sb$_{0.1}$ to 2852 m s^{-1} for Mg$_2$Sn$_{0.8}$(Sb$_{0.5}$Bi$_{0.5}$)$_{0.2}$, accompanied by a progressive reduction in κ_L, which declines from 3.4 W m^{-1} K^{-1} for Mg$_2$Sn$_{0.8}$Sb$_{0.2}$ to 1.8 W m^{-1} K^{-1} for Mg$_2$Sn$_{0.8}$(Sb$_{0.5}$Bi$_{0.5}$)$_{0.2}$ (Figures S9, Supporting Information). Debye–Callaway analysis reveals that the dominant contribution to the reduced κ_L stems from point defect scattering, consistent with behaviors observed in Bi-containing Mg$_2$Sn-based TE materials. The κ_L of our samples is slightly higher than that of the Bi-containing counterparts, likely due to weaker point-defect scattering. This is supported by the calculated mass fluctuation parameters, where $\Gamma = 0.0445$, for Mg$_2$Sn$_{0.8}$(Sb$_{0.5}$Bi$_{0.5}$)$_{0.2}$—lower than $\Gamma = 0.0697$ for Mg$_2$Sn$_{0.8}$Bi$_{0.2}$ (Figures S10, Supporting Information). In addition, the reduction in κ_L can be attributed to the disorder induced by increased entropy, which serves as a promising strategy for optimizing TE performance.[54–56] Figure 2f illustrates the significant reduction in κ_L with increasing configurational entropy (ΔS). As ΔS increases from 5.3 to 7.0 J mol^{-1} K^{-1}, the κ_L decreases from 5.8 W m^{-1} K^{-1} in Mg$_2$Sn to 1.8 W m^{-1} K^{-1} in Mg$_2$Sn$_{0.8}$(Sb$_{0.5}$Bi$_{0.5}$)$_{0.2}$. To further enhance the entropy could effectively reduce the κ_L to ≈0.8 W m^{-1} K^{-1}.[23] However, this study lies in achieving the optimum compromise of electrical and thermal transport, and the optimized ZT achieved in this work is 1.4, which is higher than the 1.3 reported for high-entropy systems in previous studies.[23] In addition, this trend also aligns with lattice softening and enhanced phonon scattering due to Bi doping,[57] which is more pronounced than that observed with Sb doping[40] in Mg$_2$Sn-based TE materials. Introducing chemical complexity and disorder by Bi can significantly influence lattice dynamics, electronic structure, and thermal conductivity. Specifically, Bi has a much larger atomic mass (208.98 u) compared to Sb (121.76 u), leading to a significant increase in the mass fluctuation parameter.[24,58] Moreover, the atomic radius of Bi (160 pm) is notably larger than that of Sb (140 pm), which increases the strain fluctuation parameter through greater lattice mismatch, further amplifying phonon scattering.[57]

These combined effects result in a pronounced reduction in κ_L while preserving favorable electrical properties, ensuring a favorable trade-off between thermal and electrical transport. The quality factor B is widely used to assess the combined influence of electron and phonon transport, highlighting the compositional optimization for peak thermoelectric performance:[51]

$$B = \left(\frac{k_B}{e}\right)^2 \frac{8\pi e\left(2m_e k_B T\right)^{3/2}}{3h^3}\frac{\mu_w}{\kappa_L}T \tag{2}$$

Here, we also use this parameter B to quantify variations in material performance. The highest B value of 0.9 is observed in Mg$_2$Sn$_{0.8}$(Sb$_{0.5}$Bi$_{0.5}$)$_{0.2}$ which is higher than the value of 0.7 in Mg$_2$Sn$_{0.8}$Sb$_{0.2}$ (Figure S11, Supporting Information), resulting in a maximum ZT of 1.4 for Mg$_2$Sn$_{0.8}$(Sb$_{0.5}$Bi$_{0.5}$)$_{0.2}$ (Figure 1c).

2.3. Interface Performance

To validate the exceptional performance of the Mg$_2$Sn$_{0.8}$(Sb$_{0.5}$Bi$_{0.5}$)$_{0.2}$ TE material, the TE device was fabricated using Cu as the electrode material. Note that Cu may not be optimal in terms of interfacial robustness; it provides a practical adopted platform for evaluating the optimized Mg$_2$Sn-based TE materials.[43,59,60] **Figure 3a** shows the characterization of the interface resistance of the n-type single-leg. After polishing the

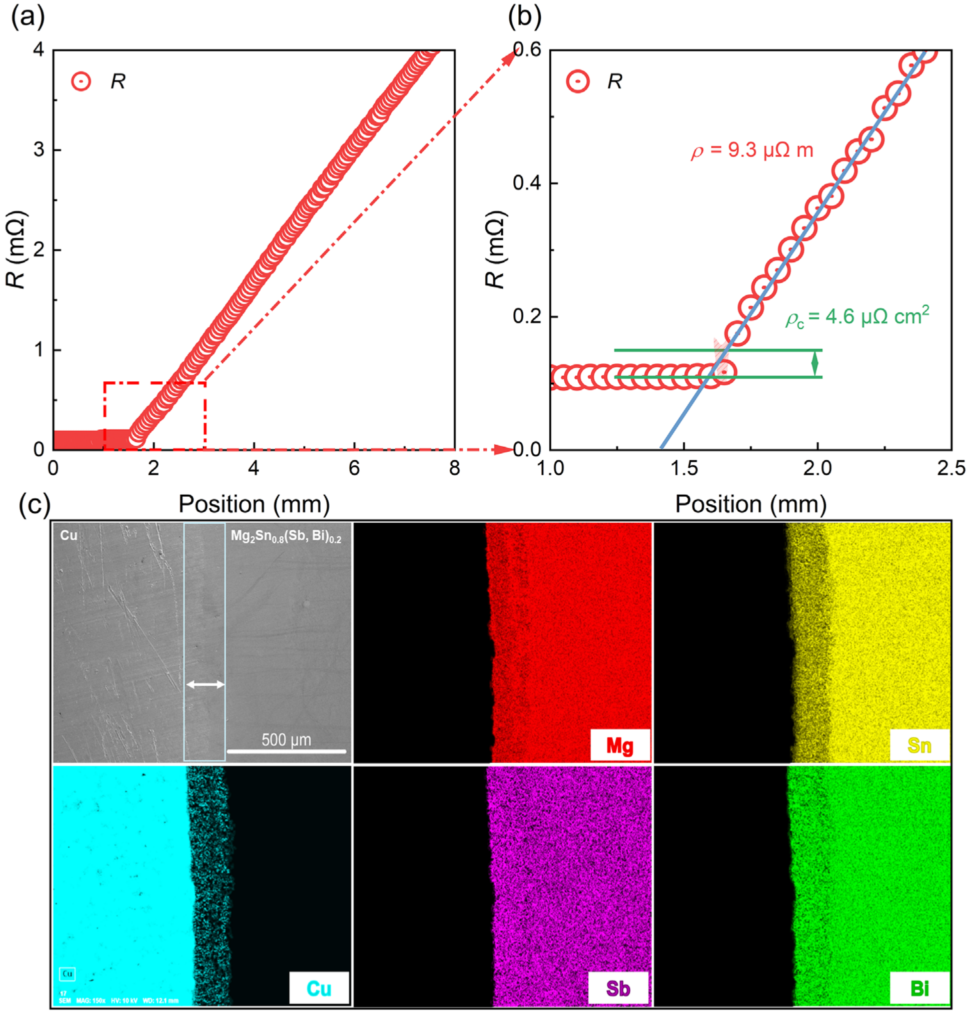

Figure 3. Electrical and microstructural characteristics of the $Mg_2Sn_{0.8}(Sb_{0.5}Bi_{0.5})_{0.2}$-based material and electrode interface. a) Resistance *R* versus position curve, with the inset showing an optical photograph of the single-leg device. b) Magnified view of the interface region in (a), highlighting the interface resistance determined from the resistance jump across the probe displacement. c) Scanning electron microscopy (SEM) image and corresponding energy dispersive spectroscopy (EDS) elemental maps of the interface region depicted in (a).

interface region, the resistance-displacement curve was used to calculate the interface resistivity (ρ_c). Notably, the transition region of the interface shows no significant resistance jumps, indicating acceptable electrical contact. A closer examination of the interface region in Figure 3b reveals a low ρ_c of 4.6 μΩ cm^2. Additionally, the ρ of the $Mg_2Sn_{0.8}(Sb_{0.5}Bi_{0.5})_{0.2}$ was determined to be 9.3 μΩ m using a scanning probe method, which closely matches the value of 8.9 μΩ m obtained from ZEM measurements. This consistency demonstrates the reliability of the measurement system and confirms that the TE material retains its optimized electrical properties even after contact fabrication.

Microstructural analysis of the interface region was performed to further elucidate the underlying mechanisms. As shown in Figure 3c, the SEM image highlights a well-bonded interface without noticeable voids or cracks, confirming the high-quality fabrication process. However, EDS elemental mapping reveals an obvious interdiffusion of elements, with a diffusion length of ≈100 μm. This level of interdiffusion is consistent with prior reports using Cu as a thermoelectric interface material.[61] The Cu is considered beneficial to its beneficial to n-type transport behavior,[62] which would not excessively deteriorate the n-type TE performance shortly. Thus, this diffusion has limited effects on both the interface and the TE performance of the material over short durations.

According to Xiong et al.[13] The device ZT_D and material ZT can be quantitatively correlated by considering the ρ of TE material, ρ_c, and device height L. They report that an ρ_c below 5 μΩ cm^2 maintains more than 95% of the material ZT, for a 2 mm Bi_2Te_3 device.

$$ZT_D = \frac{L}{(L + 2\rho_c\sigma)} ZT \tag{3}$$

Therefore, the ρ_c reported in this work is well within this ideal range. Besides, the interface of p-type $Ti/Ge_{0.9}Sb_{0.1}Te$ also exhibits a low ρ_c of < 5 μΩ cm^2 (Figures S12 and S13, Supporting Information). Note that this work aims to establish the consis-

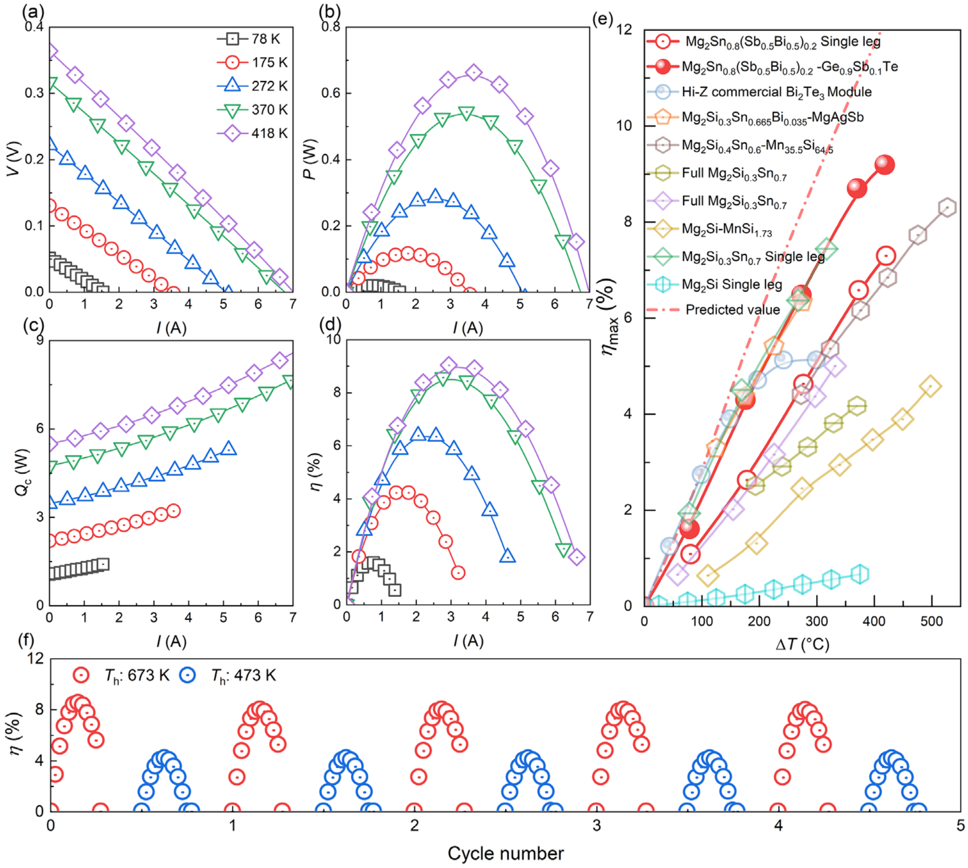

Figure 4. The power generation performance of the $Mg_2Sn_{0.8}(Sb_{0.5}Bi_{0.5})_{0.2}$-$Ge_{0.9}Sb_{0.1}Te$ module. Panels a–d) illustrate the Voltage V, Output power P, Heat flow at the cold side Qc, and Conversion efficiency η as a function of current I under various temperature differences ΔT, respectively. e) Maximum conversion efficiency η_{max} as a function of temperature difference ΔT, compared to other reported Mg_2Sn-based TE devices,[42–47,64] f) η with the cycle number, T_h cycling at 473–673 K.

tency between the material and device and does not yet include the design or optimization of diffusion barriers for long-term interfacial stability. Future studies could explore electrode interface stability, with further optimization through alloying strategies,[61] phase diagram-guided material selection,[8] or self-optimizing contact design.[63]

2.4. Device Performance

We paired n-type $Mg_2Sn_{0.8}(Sb_{0.5}Bi_{0.5})_{0.2}$ with p-type $Ge_{0.9}Sb_{0.1}Te$ in this work for the first time and conducted power generation tests under various temperature gradients to validate the device's performance. The V–I characteristics exhibit linear discharge curves at various temperature differences (ΔT), with a negative slope indicative of power generation behavior (**Figure 4a**). This linearity confirms good ohmic contact across the device under all operating conditions. The open-circuit voltage increases from 0.05 V at $\Delta T = 78$ K to 0.36 V at $\Delta T = 418$ K. At the same ΔT, the output power initially increases with current, reaching a maximum when internal resistance equals the load resistance, and then decreases with further increases in current. As shown in Figure 4b, the maximum output power rises with increasing temperature difference, reaching 0.67 W at $\Delta T = 418$ K. Similarly, the heat flow increases with current (Figure 4c), with contributions from both Joule heat and Fourier heat. The rise in open-circuit heat flow across different ΔT is mainly attributed to Fourier heat transfer. Figure 4d illustrates the conversion efficiency (η) as a function of current, displaying a parabolic trend where η initially increases with current before declining. The η_{max} improves with increasing ΔT, reaching 9% under the ΔT of 418 K (Figure 4e). We also fabricated $Mg_2Sn_{0.8}(Sb_{0.5}Bi_{0.5})_{0.2}$ single-leg devices for validation, and its η_{max} is 7.3% under the ΔT of 420 K (Figure S14, Supporting Information), slightly lower than the 7.5% reported by Chen et al.[45] However, compared to other reported TE modules involving the n-type Mg_2Sn-based with alternative p-type TE materials,[42–47,64] this combination achieves a high η_{max}, underscoring its potential for practical TE applications. In addition, the single-leg GeTe device demonstrated a conversion efficiency of 8.8% under a temperature gradient of 421 K (Figure S15, Supporting Information). Measured performance from the PEM mini system deviates from theoretical predictions (Figure S16, Supporting Information), likely due to parasitic line resistance during assembly and overestimated heat flux from radiative losses.[65] Moreover, the device exhibits acceptable cycling stability, with no noticeable η degradation observed after five thermal cycles between 473 and 673 K (Figure 4f), as well as the output power (Figures S17, Supporting Information). Note that device performance is intrinsically governed by material TE properties, including power factor, *ZT*, as well as external factors such as device sized, ρ_c, and temperature gradient. Herein, we focus on materials properties and demonstrate that balancing power factors and thermal conductivity via a stepwise Sb-Bi aliovalent solid solution strategy enables high efficiency in intrinsically high power density thermoelectric modules.

3. Conclusion

This work presents a novel combination of Mg_2Sn and GeTe, intrinsically high-power-density devices that have not been previously explored. Our design approach addresses the challenge of efficiency limitations due to their usually high thermal conductivity by incorporating aliovalent Sb and Bi solid solutions in Mg_2Sn, which effectively reduces thermal conductivity while retaining the power factor. This results in a lattice thermal conductivity of 1.8 W m^{-1} K^{-1} and a peak *ZT* of 1.4 in $Mg_2Sn_{0.8}(Sb_{0.5}Bi_{0.5})_{0.2}$. The Mg_2Sn-GeTe module achieves a η_{max} of 9% at a high power density of 0.7 W·cm^{-2} under a 418 K temperature gradient, offering a promising strategy for efficient thermal energy conversion and advancing the development of sustainable energy solutions in intrinsically high-power-density TEG.

4. Experimental Section

Materials Synthesis: The $Mg_{2.06}Sn_{0.9}Sb_{0.1}$, $Mg_{2.06}Sn_{0.8}Sb_{0.2}$, $Mg_{2.06}Sn_{0.8}(Sb_{0.5}Bi_{0.5})_{0.2}$, and $Mg_{2.06}Sn_{0.7}Sb_{0.3}$ compounds were synthesized using high-purity magnesium turnings (99.95%), tin shots (99.99%), antimony shots (99.999%), and bismuth shots (99.999%). Excess magnesium is denoted as Mg_2 in the text, with similar abbreviations for other compositions. For example, $Mg_{2.06}Sn_{0.9}Sb_{0.1}$ is denoted as $Mg_2Sn_{0.9}Sb_{0.1}$. The raw materials were weighed according to their stoichiometric ratios and mechanically alloyed for 7 h using an SPEX-8000D high-energy mill under an argon atmosphere. The resulting powders were consolidated into bulk samples via vacuum spark plasma sintering at 873 K and 60 MPa for 5 min using the SPS-1080 System (SPS SYNTEX INC). The $Ge_{0.9}Sb_{0.1}Te$ samples, bulk Ge (99.99%), Te (99.99%), and Sb (99.99%) were weighed stoichiometrically and sealed in evacuated quartz tubes. The tubes were gradually heated to 1323 K, held at this temperature for 20 h to ensure complete mixing and reaction, and then cooled to room temperature. The alloys obtained were ground into fine powders using an agate mortar and consolidated by SPS under an axial pressure of 60 MPa at 873 K for 10 min (SPS-322Lx, Dr. Sintering).

Characterization and Measurements: The phase and phase transitions were investigated using a X-ray diffractometer (Rigaku SmartLab 9 kW). The electrical transport properties, including *S* and the σ, were measured by ZEM-3 (Advance Riko, ± 5% uncertainty), and the thermal transport property κ was calculated by the formula: $\kappa = D\rho C_p$, where the *D* represents thermal diffusivity and was measured by LFA467 (Netzsch, ±3% uncertainty). The sample density ρ and C_p were obtained by the Archimedes method and Dulong-Petit law. The Hall measurements were performed using a Quantum Design Physical Property Measurement System. The magnetic field was swept from −4 T to +4 T at room temperature. The Hall coefficient R_H was extracted from the slope of the linear fit of Hall resistance versus magnetic field. The carrier concentration *n* and Hall mobility μ_H were calculated using the relation $n = 1/(eR_H)$ and $\mu = \sigma R_H$, where *e* is the elementary charge. The contact resistance of the TE junctions was measured by a two-axis resistance distribution measurement instrument (S1331, Mottainai Energy). The thermoelectric modules were tested by the commercial instrument Mini-PEM (Advance Riko).

TE Device Fabrication and Simulation: The $Mg_2Sn_{0.8}(Sb_{0.5}Bi_{0.5})_{0.2}$ TE leg was fabricated by sandwiching two layers of Cu powders as interface materials, followed by SPS (SPS-322Lx, Dr. Sintering) at 873 K and 60 MPa for 5 min. The sintered TE legs were then cut into dice with dimensions of $\approx 3.8 \times 3.8 \times 6.5$ mm^3. Two-pair TE modules were constructed using these p-type $Ge_{0.9}Sb_{0.1}Te$ legs and n-type $Mg_2Sn_{0.8}(Sb_{0.5}Bi_{0.5})_{0.2}$ TE legs. A Ti diffusion barrier layer was introduced at the GeTe side to suppress interfacial reactions. The dimensions of the two-pair TE module are $\approx 10 \times 10 \times 10$ mm^3, with the AlN ceramic plate and copper electrode being 0.635 and 0.2 mm, respectively. Finite-element simulations were performed using COMSOL Multiphysics to model both the single-leg and two-pair TE devices.

Supporting Information

Supporting Information is available from the Wiley Online Library or from the author.

Acknowledgements

X.W., L.W., and A.L. contributed equally to this work. The authors acknowledge support from JST Mirai Large-Scale Program JPMJMI19A1. Institutional support from the JSPS WPI Academy Program is also acknowledged.

Conflict of Interest

The authors declare no conflict of interest.

Author Contributions

Xinzhi Wu wrote the original manuscript. Takao Mori designed the project. Xinzhi Wu, Longquan Wang, and Airan Li prepared the samples and carried out the measurements. Xinzhi Wu, Gang Wu, Zhao Hu, and Fei Frank Yun analyzed the data. Takao Mori supervised the whole project. All the authors discussed, reviewed, and edited the manuscript.

Data Availability Statement

The data that support the findings of this study are available from the corresponding author upon reasonable request.

Keywords

conversion efficiency, Mg2Sn-GeTe device, power density, thermoelectric generators

Received: April 19, 2025
Revised: July 4, 2025
Published online: July 30, 2025

[1] G. Schierning, *Nat. Energy* **2018**, *3*, 92.
[2] C. Zhao, S. Ju, Y. Xue, T. Ren, Y. Ji, X. Chen, *Carbon Neutrality* **2022**, *1*, 7.
[3] S. Chu, A. Majumdar, *Nature* **2012**, *488*, 294.
[4] T. Mori, A. Maignan, *Sci. Technol. Adv. Mater.* **2021**, *22*, 998.
[5] A. Li, Y. Wang, Y. Li, X. Yang, P. Nan, K. Liu, B. Ge, C. Fu, T. Zhu, *Nat. Commun.* **2024**, *15*, 5108.
[6] Q. H. Zhang, K. F. Deng, L. Wilkens, H. Reith, K. Nielsch, *Nat. Electron.* **2022**, *5*, 333.
[7] Y. F. Xing, R. H. Liu, J. C. Liao, C. Wang, Q. H. Zhang, Q. F. Song, X. G. Xia, T. J. Zhu, S. Q. Bai, L. D. Chen, *Joule* **2020**, *4*, 2475.
[8] L. J. Xie, L. Yin, Y. Yu, G. Y. Peng, S. W. Song, P. J. Ying, S. T. Cai, Y. X. Sun, W. J. Shi, H. Wu, N. Qu, F. K. Guo, W. Cai, H. J. Wu, Q. Zhang, K. Nielsch, Z. F. Ren, Z. H. Liu, J. H. Sui, *Science* **2023**, *382*, 921.
[9] J. Camut, N. H. Pham, D. Y. Nhi Truong, G. Castillo-Hernandez, N. Farahi, M. Yasseri, E. Mueller, J. de Boor, *Mater. Today Energy* **2021**, *21*, 100718.
[10] G. K. Goyal, T. Dasgupta, *ACS Appl. Mater. Interfaces* **2021**, *13*, 20754.
[11] B. Jayachandran, B. Prasanth, R. Gopalan, T. Dasgupta, D. Sivaprahasam, *Mater. Res. Bull.* **2021**, *136*, 111147.
[12] R. Chetty, J. Babu, T. Mori, *ACS Appl. Energy Mater.* **2024**, *7*, 12112.
[13] K. Xiong, W. Wang, H. N. Alshareef, R. P. Gupta, J. B. White, B. E. Gnade, K. Cho, *J. Phys. D: Appl. Phys.* **2010**, *43*, 115303.
[14] S. Harish, D. Sivaprahasam, B. Jayachandran, R. Gopalan, G. Sundararajan, *Energy Convers. Manage.* **2021**, *232*, 113900.
[15] F. Garmroudi, M. Parzer, A. Riss, C. Bourgès, S. Khmelevskyi, T. Mori, E. Bauer, A. Pustogow, *Sci. Adv.* *9*, adj1611.
[16] L. Chen, R. Liu, X. Shi, in *Thermoelectric Materials and Devices* (Eds: L. Chen, R. Liu, X. Shi), Elsevier, Amsterdam **2021**, pp. 81–145.
[17] N. T. Tarachand, F. Garmroudi, E. Bauer, T. Mori, *Mater. Today Phys.* **2024**, *48*, 101568.
[18] V. K. Zaitsev, M. I. Fedorov, E. A. Gurieva, I. S. Eremin, P. P. Konstantinov, A. Y. Samunin, M. V. Vedernikov, *Phys. Rev. B* **2006**, *74*, 045207.
[19] H. Ning, G. D. Mastrorillo, S. Grasso, B. Du, T. Mori, C. Hu, Y. Xu, K. Simpson, G. Maizza, M. J. Reece, *J. Mater. Chem. A* **2015**, *3*, 17426.
[20] W. S. Liu, H. S. Kim, S. Chen, Q. Jie, B. Lv, M. Yao, Z. F. Ren, *Proc. Natl. Acad. Sci. USA* **2015**, *112*, 3269.
[21] W. Liu, X. J. Tan, K. Yin, H. J. Liu, X. F. Tang, J. Shi, Q. J. Zhang, C. Uher, *Phys. Rev. Lett.* **2012**, *108*, 166601.
[22] G. Jiang, J. He, T. Zhu, C. Fu, X. Liu, L. Hu, X. Zhao, *Adv. Funct. Mater.* **2014**, *24*, 3776.
[23] H. Gao, K. Zhao, H. Wuliji, M. Zhu, B. Xu, H. Lin, L. Fei, H. Zhang, Z. Zhou, J. Lei, *Energy Environmental Science* **2023**, *16*, 6046.
[24] A. U. Khan, N. Vlachos, T. Kyratsi, *Scr. Mater.* **2013**, *69*, 606.
[25] A. Sankhla, A. Patil, H. Kamila, M. Yasseri, N. Farahi, E. Mueller, J. de Boor, *ACS Appl. Energy Mater.* **2018**, *1*, 531
[26] W. Saito, K. Hayashi, Z. Huang, K. Sugimoto, K. Ohoyama, N. Happo, M. Harada, K. Oikawa, Y. Inamura, K. Hayashi, T. Miyazaki, Y. Miyazaki, *ACS Appl. Energy Mater.* **2021**, *4*, 5123.
[27] I. Ohkubo, M. Murata, A. Ohi, M. S. L. Lima, T. Sakurai, T. Aizawa, T. Mori, *Appl. Phys. Lett.* **2023**, *122*, 243901.
[28] M. Hong, W. Y. Lyv, M. Li, S. D. Xu, Q. Sun, J. Zou, Z. G. Chen, *Joule* **2020**, *4*, 2030.
[29] T. Xing, C. Zhu, Q. Song, H. Huang, J. Xiao, D. Ren, M. Shi, P. Qiu, X. Shi, F. Xu, L. Chen, *Adv. Mater.* **2021**, *33*, 2008773.
[30] S. Perumal, M. Samanta, T. Ghosh, U. S. Shenoy, A. K. Bohra, S. Bhattacharya, A. Singh, U. V. Waghmare, K. Biswas, *Joule* **2019**, *3*, 2565.
[31] Z. Liu, W. Gao, W. Zhang, N. Sato, Q. Guo, T. Mori, *Adv. Energy Mater.* **2020**, *10*, 2002588.
[32] M. Hong, K. Zheng, W. Y. Lyv, M. Li, X. L. Qu, Q. Sun, S. D. Xu, J. Zou, Z. G. Chen, *Energy Environ. Sci.* **2020**, *13*, 1856.
[33] Z. L. Bu, X. Y. Zhang, B. Shan, J. Tang, H. X. Liu, Z. W. Chen, S. Lin, W. Li, Y. Z. Pei, *Science Advance* **2021**, *7*, abf2738.
[34] B. B. Jiang, W. Wang, S. X. Liu, S. X. Wang, C. F. Wang, Y. N. Chen, L. Xie, M. Y. Huang, J. Q. He, *Science* **2022**, *377*, 208.
[35] C. Liu, Z. Zhang, Y. Peng, F. Li, L. Miao, E. Nishibori, R. Chetty, X. Bai, R. Si, J. Gao, X. Wang, Y. Zhu, N. Wang, H. Wei, T. Mori, *Sci. Adv.* **2023**, *9*, adh0713.
[36] Y. Jiang, J. Dong, H. L. Zhuang, J. Yu, B. Su, H. Li, J. Pei, F. H. Sun, M. Zhou, H. Hu, J. W. Li, Z. Han, B. P. Zhang, T. Mori, J. F. Li, *Nat. Commun.* **2022**, *13*, 6087.
[37] J. Mao, H. S. Kim, J. Shuai, Z. H. Liu, R. He, U. Saparamadu, F. Tian, W. S. Liu, Z. F. Ren, *Acta Mater.* **2016**, *103*, 633.
[38] L. Zheng, X. Zhang, H. Liu, S. Li, Z. Zhou, Q. Lu, J. Zhang, F. Zhang, *J. Alloys Compd.* **2016**, *671*, 452.
[39] A. U. Khan, N. V. Vlachos, E. Hatzikraniotis, G. S. Polymeris, C. B. Lioutas, E. C. Stefanaki, K. M. Paraskevopoulos, I. Giapintzakis, T. Kyratsi, *Acta Mater.* **2014**, *77*, 43.
[40] B. Wang, H. Zhao, J. Li, B. Zhang, D. Wang, C. Chen, A. Song, W. Hu, D. Yu, B. Xu, Y. Tian, *J. Materiomics* **2023**, *10*, 285.
[41] A. Mehdizadeh Dehkordi, M. Zebarjadi, J. He, T. M. Tritt, *Mater. Sci. Eng. R: Rep.* **2015**, *97*, 1.
[42] H. S. Kim, K. Kikuchi, T. Itoh, T. Iida, M. Taya, *Mater. Sci. Eng., B* **2014**, *185*, 45.
[43] G. K. Goyal, T. Dasgupta, *Mater. Sci. Eng., B* **2021**, *272*, 115338.
[44] J. Chen, W. H. Fan, Y. C. Wang, Y. Jiang, S. Ohno, Z. A. Munir, M. Ferhat, S. p. Chen, *J. Alloys Compd.* **2022**, *926*, 166888.
[45] K. Cheng, Z. L. Bu, J. Tang, X. Y. Zhang, X. Meng, W. Li, Y. Z. Pei, *Mater. Today Phys.* **2022**, *28*, 100887.
[46] J. Camut, P. Ziolkowski, P. Ponnusamy, C. Stiewe, E. Mueller, J. de Boor, *Adv. Eng. Mater.* **2023**, *25*, 2200776.
[47] A. Wieder, J. Camut, A. Duparchy, R. Deshpande, A. Cowley, E. Müller, J. de Boor, *Mater. Today Energy* **2023**, *38*, 101420.
[48] A. Li, L. Wang, J. Li, T. Mori, *Energy Environ. Sci.* **2024**, *17*, 8810.
[49] Y. B. Zhu, E. T. Dong, Z. J. Han, F. Jiang, J. H. Sui, W. Q. Zhang, W. S. Liu, *Acta Mater.* **2021**, *217*, 117172.
[50] Y. Zhu, Z. Han, F. Jiang, E. Dong, B. P. Zhang, W. Zhang, W. Liu, *Mater. Today Phys.* **2021**, *16*, 100327.
[51] G. J. Snyder, A. H. Snyder, M. Wood, R. Gurunathan, B. H. Snyder, C. Niu, W. Mobility, *Adv. Mater.* **2020**, *32*, 2001537.
[52] K. Imasato, S. D. Kang, G. J. Snyder, *Energy Environ. Sci.* **2019**, *12*, 965.
[53] C. Hu, K. Xia, C. Fu, X. Zhao, T. Zhu, *Energy Environ. Sci.* **2022**, *15*, 1406.
[54] S. Ghosh, A. Nozariasbmarz, H. Lee, L. Raman, S. Sharma, R. B. Smriti, D. Mandal, Y. Zhang, S. K. Karan, N. Liu, J. L. Gray, M. Sanghadasa, Y. Xia, S. Priya, W. Li, B. Poudel, *Joule* **2024**, *8*, 3303.
[55] R. H. Liu, H. Y. Chen, K. P. Zhao, Y. Qin, B. B. Jiang, T. Zhang, G. Sha, X. Shi, C. Uher, W. Q. Zhang, L. D. Chen, *Adv. Mater.* **2017**, *29*, 201702712.
[56] B. B. Jiang, Y. Yu, J. Cui, X. Liu, L. Xie, J. Liao, Q. Zhang, Y. Huang, S. Ning, B. Jia, B. Zhu, S. Q. Bai, L. D. Chen, S. J. Pennycook, J. Q. He, *Science* **2021**, *371*, 830.
[57] H. Zhao, D. Wang, B. Wang, A. Song, C. Chen, W. Hu, D. Yu, B. Xu, Y. Tian, *J. Alloys Compd.* **2024**, *987*, 174215.
[58] P. Mangelis, A. Sousanis, G. Mesaritis, P. S. Ioannou, A. K. Søiland, Y. Xu, T. Kyratsi, *ACS Appl. Electron. Mater.* **2024**, *6*, 2988.
[59] J. S. Graff, R. Schuler, X. Song, G. Castillo-Hernandez, G. Skomedal, E. Enebakk, D. N. Wright, M. Stange, J. de Boor, O. M. Lovvik, M. Schrade, *J. Electron. Mater.* **2021**, *50*, 4041.
[60] K. Singsoog, P. Pilasuta, S. Paengson, W. Namhongsa, S. Ruamruk, T. Seetawan, *Materials Today-Proceedings* **2019**, *17*, 1437.
[61] X. Z. Wu, Y. J. Lin, C. Y. Liu, Z. J. Han, H. Li, Y. P. Wang, F. Jiang, K. Zhu, B. H. Ge, W. S. Liu, *Adv. Energy Mater.* **2023**, *13*, 2301350.

[62] M. Safavi, N. Martin, E. Aubry, V. Linseis, A. Billard, M. Arab Pour Yazdi, *J. Electron. Mater.* **2021**, *50*, 2738.

[63] A. Li, L. Wang, J. Li, X. Wu, T. Mori, *Nat. Commun.* **2025**, *16*, 1502.

[64] H. Kaibe, I. Aoyama, M. Mukoujima, T. Kanda, S. Fujimoto, T. Kurosawa, H. Ishimabushi, K. Ishida, L. Rauscher, Y. Hata, S. Sano, *ICT 2005. 24th International Conference on Thermoelectrics*, IEEE, Clemson, SC, USA **2005**, 242.

[65] R. Chetty, J. Babu, T. Mori, *Joule* **2024**, *8*, 556.